



Jiun-Jih Miao · Shang-Ru Li · Zong-Xiu Tsai · Mai Van Phung · San-Yi Lin

On the aerodynamic flow around a cyclist model at the hoods position

Received: 16 May 2019 / Revised: 30 July 2019 / Accepted: 5 September 2019 / Published online: 9 October 2019
© The Author(s) 2019

Abstract Aerodynamic flow around an 1/5 scale cyclist model was studied experimentally and numerically. First, measurements of drag force were performed for the model in a low-speed wind tunnel at Reynolds numbers from 5.5×10^4 to 1.8×10^5 . Meanwhile, numerical computation using a large eddy simulation method was performed at three Reynolds numbers of 1.1×10^4 , 6.5×10^4 and 1.5×10^5 to obtain the drag coefficients for comparison. Second, flow visualization was made in a water channel and the wind tunnel mentioned to examine the three-dimensional flow separation pattern on the model surface, which could also be realized from the numerical results. Finally, a wake flow survey based on the hot-wire measurements in the wind tunnel showed that in the near-wake region, the flow was featured with the formation of multiple streamwise vortices. The numerical results further indicated that these vortices were evolved from the separated flows occurred on the model surface.

Keywords Cycling aerodynamics · Flow visualization · Flow separation · Drag · Wake

1 Introduction

When cycling at reasonably high speed, the drag due to a cyclist can be much greater than that resulted from the bicycle being ridden. Evidence reported in the literature indicates that during cycling at a racing speed of 50 km/h, aerodynamic drag can contribute about 90% of the total drag (Kyle and Burke 1984), of which 70% is due to the cyclist. Therefore, it would be more effective to reduce the drag due to the cyclist than that of the bicycle.

The drag experienced by a cyclist is associated with a complicated aerodynamic flow around a three-dimensional contoured body, for which the phenomenon of flow separation plays a significant role. As noted in the literature (Lukes et al. 2005; Defraeye et al. 2010a, b, 2011; Blocken et al. 2018), the aerodynamic flow is strongly dependent upon the posture of a cyclist. Defraeye et al. (2010a) conducted a numerical and experimental study for a cyclist at the upright, dropped and time trial positions, respectively. Experiments were made in a large-scale wind tunnel that a cyclist with a racing bicycle was situated in the test section for aerodynamic drag measurements. In addition, there were 30 pressure plates (sensors) applied on the cyclist's body to collect the instantaneous pressure measurements. Meanwhile, numerical simulations were carried out for the cases studied. Accordingly, the numerical and experimental results on the values of drag area and the pressure coefficients at different locations on the cyclist body were compared. Overall speaking, the results obtained by the two approaches were in good agreement, which inferred that the method of numerical

simulation can be of use to study cycling aerodynamics. As they pointed out, using the numerical simulation method could provide the information of the flow in a more cost-effective manner, compared to using the experimental approach. Defraeye et al. (2010b) conducted the numerical simulations of flow around a cyclist with testing the turbulence models available in the literature. The numerical results of pressure distribution obtained were then compared with the experimental data of a half-sized cyclist model at 115 locations, which were obtained from wind tunnel testing. It was concluded that the RANS SST $k-\omega$ model gave the best overall performance among the models tested. Later, Defraeye et al. (2011) extended the numerical simulation to analyze the drag and convective heat transfer corresponding to the individual segments of a cyclist model, that the cyclist model was divided into 19 segments. The numerical results of drag and convective heat transfer corresponding to each of the segments at the upright, dropped and time trial positions were examined. As found, the high drag area values were attributed to the segments of head, legs and arms. Furthermore, it was noted that the aerodynamic drag of each segment was strongly dependent upon the cyclist posture, but the convective heat transfer was less sensitive.

A group of studies were concerned with the drag of a cyclist in dynamic motions. Griffith et al. (2014) pointed out that the leg motion affected the aerodynamic drag significantly, and the transient case under consideration would represent a situation close to the reality than a steady case. Crouch et al. (2014, 2016a, b) conducted a series of studies on the effect of pedaling with regard to a cyclist at the time trial position. In the wind tunnel experiments with a full scale mannequin (Crouch et al. 2014), the data of total drag measurements and pressure measurements on the body surface together with the velocity measurements in the wake region unveiled that the three-dimensional flow distribution around the mannequin varied with pedaling at different crank angles. As noted, the flow with significant momentum deficit in the turbulent wake behind the hip played a predominant role in the development of unsteady flow around the cyclist body.

The flow phenomenon around multi-cyclists has been concerned greatly in the competition of team pursuit cycling. Blocken et al. (2013) conducted numerical analysis of flow around two drafting cyclists with different separation distance. Based on the numerical findings, discussion on the strategy of reducing the total drag was carried out. Defraeye et al. (2014) performed numerical simulations for four cyclists in a pace line with different postures and variable separation distances. Based on the results of the cases studied, the drag forces resulted from different segments of the bodies of the cyclists were examined. The aim of the work was to evaluate the reduction in the total drag subjected to the flow conditions specified.

In discussing the cyclist drag, a quantity called the drag area (Defraeye et al. 2010a) or the effective frontal area (Debraux et al. 2011) as the product of the drag coefficient and the frontal area is frequently referred. An obvious reason of using this quantity is that it can be obtained directly from the drag force measured and subsequently divided by the dynamic pressure based on the characteristic velocity. Nevertheless, as far as the strategy of reducing the drag is concerned, it would be better to examine the two quantities separately, since each of which has its own physical significance. The frontal area is realized to be critically dependent upon the posture of the cyclist. To determine the frontal area of a cyclist in laboratory or actual racing situations is not trivial. For instance, Debraux et al. (2011) reviewed the methods for the determination of the frontal area of a cyclist. On the other hand, the drag coefficient is a non-dimensional quantity representing the aerodynamic characteristics of concern. In general, it can be referred to as an indicator concerning the bluffness of an aerodynamic body. A cyclist is regarded as a blunt body since a large portion of the drag produced is associated with the form drag. For a cyclist at a fixed posture, the drag coefficient may vary with the Reynolds number (Defraeye et al. 2010a, 2011) as well as the surface roughness as introduced by the sportware (Oggiano et al. 2007, 2009; Chowdhury and Alam 2014; Hsu et al. 2019).

This study is focused on the aerodynamic flow around a cyclist model at the hoods position, a posture applying to a wide range of speed (4.2–12.5 m/s) in cycling. An 1/5 scale cyclist model was employed for experiment with using the methods of flow visualization, force measurement and wake flow survey. Moreover, the numerical simulation was made to obtain the flow distribution around the cyclist model. The numerical results were of use to complement the experimental findings and to assist in explaining the complicated flow phenomenon around the cyclist model.

2 Methodology

2.1 The cyclist model

The cyclist model at the hoods position for experiment is shown in Fig. 1a. It is an 1/5 scale model made by a 3D printer, whose surface data were provided by GIANT Inc., Taiwan. The dimension of the model is further given in Fig. 1b. Notably, the inclination angle of the upper body of the model, α , is 32° . The torso length, C , is 110 mm; C is denoted as the reference length in this study. The crank angle, $\theta = 195^\circ$, is associated with the foot positions of the model. The frontal area of the model called A_C is 0.0122 m^2 , excluding that of the sting support.

The Cartesian coordinate system employed in this study is shown in Fig. 1b with the origin located at the root of the sting support; x , y and z denote the streamwise, lateral and vertical directions, respectively. In this study, the instantaneous, time mean, fluctuating and root-mean-square velocities in the x , y and z directions are denoted as $(u, \bar{u}, u', u'_{\text{rms}})$, $(v, \bar{v}, v', v'_{\text{rms}})$ and $(w, \bar{w}, w', w'_{\text{rms}})$, respectively.

2.2 Water channel experiments

In this work, a water channel facility was employed for the experiments of flow visualization and PIV velocity measurements. The test section of the water channel was 0.6 m in width, 0.6 m in height and 2.5 m in length. The cyclist model was situated 1 m downstream from the inlet of the test section, where the freestream turbulent intensity was about 1%. The blockage ratio of the model was 5.9%. Experiments were made at the Reynolds number, Re_C , about 1.1×10^4 , where Re_C is based on C , and the incoming velocity, U_∞ .

An arrangement for PIV system is shown in Fig. 2a, where the cyclist model was positioned upside down. The PIV system employed was capable of measuring two components of the flow velocity, with an Argon ion laser as the light source. A sketch of the model included in this figure provides an indication of the central plane, $y/C = 0$, where the PIV velocity measurements were performed. The measurements were made by taking 2000 images continuously at a rate of 200 fps. In addition, flow visualization in the water channel was conducted with the ink dots and dye-injection methods.

2.3 Wind tunnel experiments

An open-jet low-speed wind tunnel employed for the present study is shown in Fig. 2b. The cyclist model was situated in an extended test section of 0.5 m in diameter, that the area blockage ratio of the model was 6.8%. The flow speed in the test section could reach 35 m/s, at which the freestream turbulence intensity measured was less than 0.7%. The incoming velocity U_∞ was monitored by a Pitot tube located immediately downstream of the inlet. Further, this figure provides a schematic view depicting an X-type hot-wire probe situated on a 3-D traversing mechanism for conducting the velocity measurements in the wake behind the cyclist model.

The hot-wire velocity measurements were carried out at six streamwise locations indicated in a sketch included in Fig. 2b. Specifically, in the cross-sectional planes of $x/C=0.8, 1.2, 1.6, 2.0$ and 2.4 , the hot-wire

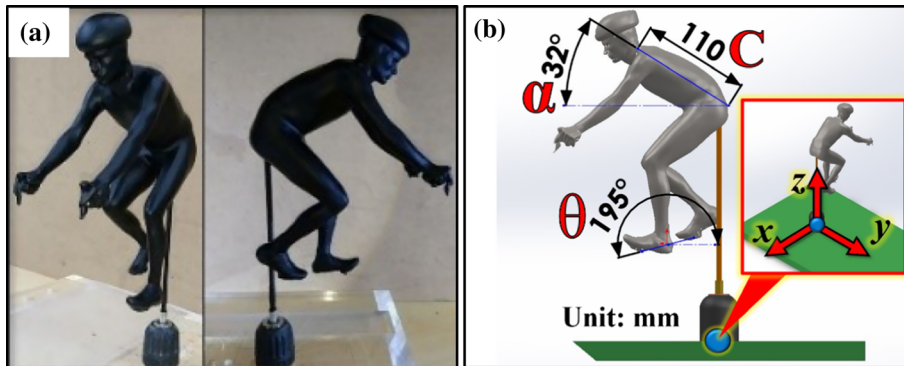


Fig. 1 a An 1/5 scale cyclist model employed for experiment, b the model marked with the dimension and the Cartesian coordinate system employed

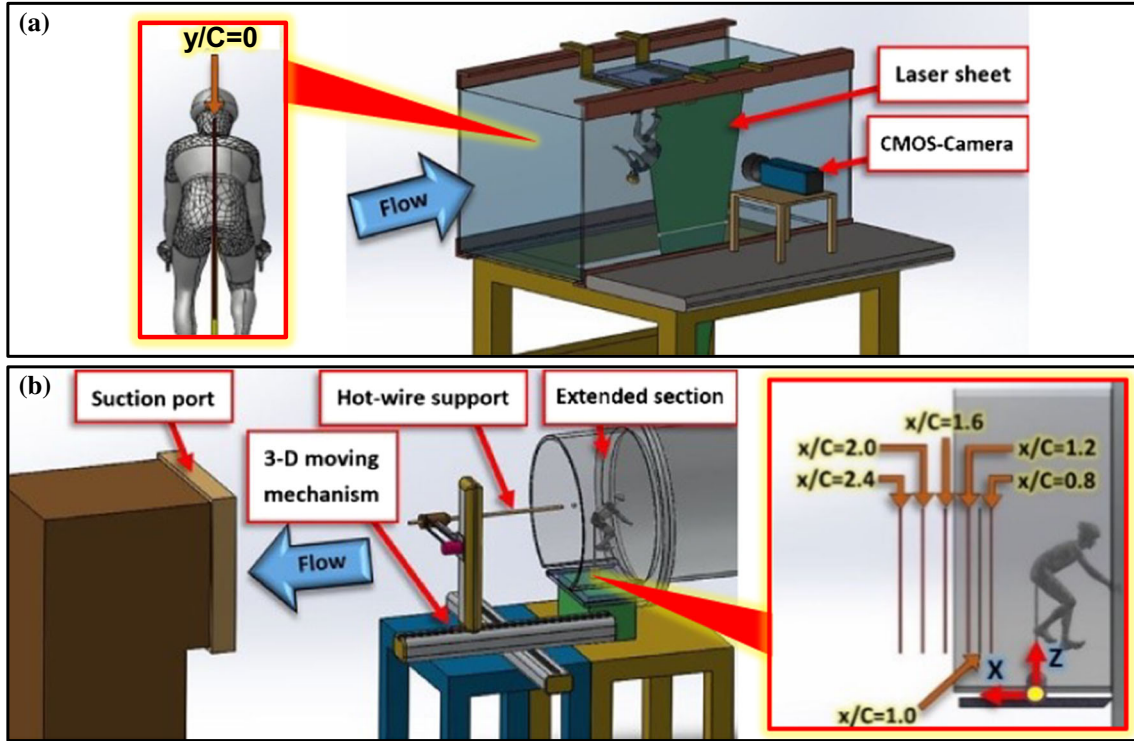


Fig. 2 **a** The experimental setup of the PIV system in a water channel, and **b** the experimental setup of the hot-wire velocimetry in a wind tunnel

velocity measurements were made at the grid points spaced by 10 mm; at each of the grid points, the hot-wire output signals of each channel were sampled at 1 kHz for 8192 samples. In addition, at $x/C = 1.0$, the velocity measurements were made with a finer grid spacing of 5 mm for a detailed survey of the wake flow. In this case, the hot-wire signals of each channel were sampled at 2 kHz for 16,384 samples. All of the measurements mentioned above were made at $Re_C = 6.5 \times 10^4$. Note that in order to obtain the flow quantities of the three-dimensional flow, the hot-wire velocity measurements at each grid point were actually made twice. The second time was made after the hot-wire probe rotated 90° .

The statistical quantities reduced from the velocity measurements are described below. The non-dimensional time mean streamwise velocity (\bar{u}^*) is defined as \bar{u}/U_∞ . The total turbulence intensity (TI_{xyz}) is defined as $[(u'_{rms}{}^2 + v'_{rms}{}^2 + w'_{rms}{}^2)/3]^{0.5}/U_\infty \times 100\%$. In addition, the non-dimensional shearing Reynolds stresses associated with the xy and xz terms (R_{xy}^* , R_{xz}^*) are defined as $\overline{u'v'}/U_\infty^2$ and $\overline{u'w'}/U_\infty^2$, respectively, which have the physical implications of transporting the momentum and kinetic energy through the respective components of turbulent fluctuations. The non-dimensional time mean streamwise vorticity ($\overline{\omega_x^*}$) is defined by $\overline{\omega_x}C/U_\infty$, where $\overline{\omega_x} = \partial\bar{w}/\partial y - \partial\bar{v}/\partial z$.

In order to identify the presence of streamwise coherent vortices in the wake region, the λ_2 -criterion (Jeong and Hussain 1995; Chen et al. 2015) was adopted in this study, whereas a different method was adopted by Crouch et al. (2014) for vortex identification in their study. One may refer to Li (2017) for more details about the discussion on the methods of vortex identification. To describe the strength of a vortex identified, a non-dimensional streamwise circulation (Γ^*) is defined as $\sum_{n=1}^N \overline{\omega_{x_n}^*} \Delta y \Delta z / A_C$, where Δy and Δz denote the spacing of the measurement grid points in the y and z directions, respectively, within the vortex region defined.

To measure the drag force experienced by the cyclist model, a self-made one-component external force balance of a platform type was employed, which is shown in Fig. 3a. The drag force of the testing model was sensed by the strain gauges on the flexure plate. More details regarding the balance design can be found in Tsai et al. (2016).

The balance was calibrated using a single-vector force calibration method (Parker et al. 2001). The 95% confidence interval (abbreviated as 95% CI) with regard to the measurement uncertainty of the balance is shown in Fig. 3b. The 95% CI was reduced according to a formula of $k\sqrt{s/n}/\bar{f}_m \times 100\%$, where \bar{f}_m and s

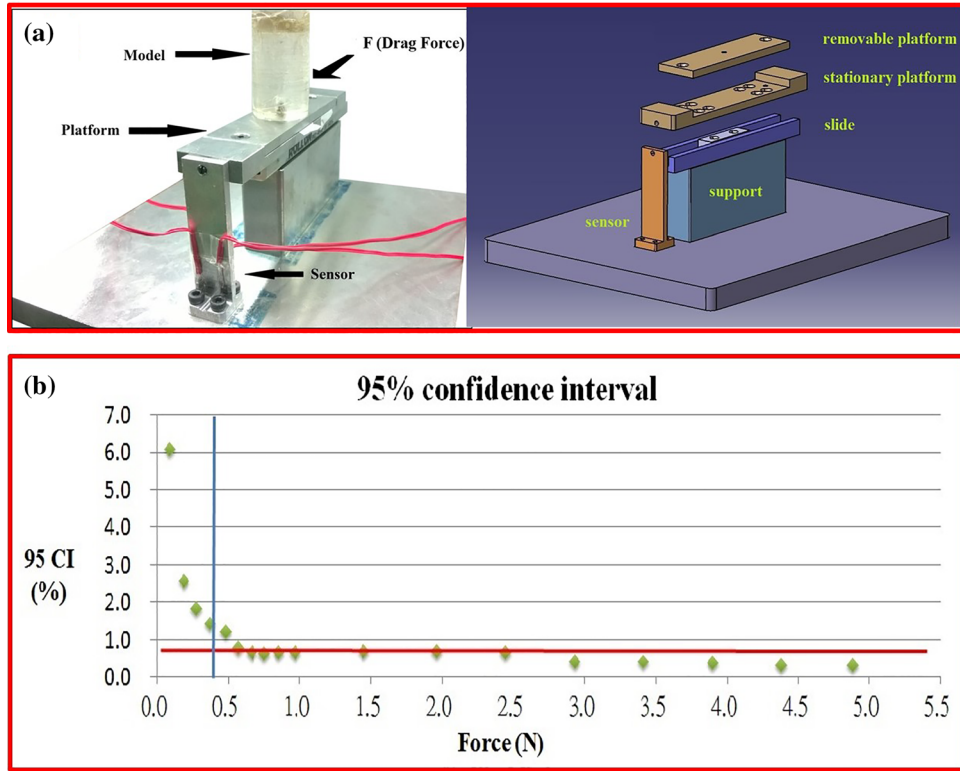


Fig. 3 **a** The self-made force balance, and **b** variations of the 95% CI (the confidence of interval) versus the applied forces

represent the average and standard deviation values corresponding to n times of the applied forces measured, respectively; $k = 2$ is assumed as n was greater than 21 (Bandet and Perisol 1991). As seen in Fig. 3b, for the applied forces above 0.6 N, the corresponding uncertainties of the balance were no more than 0.8%, indicated by a dashed line in the figure, which is comparable to that of a commercial grade balance. On the other hand, if the applied forces lower than 0.6 N, the uncertainties were increased substantially due to the impact of the background noise on the accuracy.

In this study, the balance output was sampled at 1 kHz for 120 s. The measured results were expressed in terms of the drag coefficient, C_D ; $C_D = F_D / (0.5\rho U_\infty^2 A_C)$, where F_D and ρ denote the drag force and the density of the working fluid, respectively. Apart from the self-made balance, a commercial balance of JR3, Inc., was available for the present study. Therefore, a comparison on the data obtained by the two balances was made in this study.

Flow visualization experiment using an oil film technique was conducted in the wind tunnel for revealing the limiting streamline patterns on the model surface. Details regarding this technique can be found in Li et al. (2017).

2.4 Numerical simulation

Numerical simulation of flow around the cyclist model was carried out by a large eddy simulation (LES) method using the Fluent/ANSYS software. The parameters of the simulation were defined according to the experiments made in the water channel and the wind tunnel, respectively.

In the water channel case ($Re_C = 1.1 \times 10^4$), the sub-grid scale (SGS) eddy viscosity model suggested by Smagorinsky (1963) was adopted. The Smagorinsky constant chosen was 0.16 to make the best correlation between numerical simulation and experiment (McMillan and Ferziger 1979). On the other hand, in simulating the cases of the wind tunnel experiments at higher Reynolds numbers, $Re_C = 6.5 \times 10^4$ and 1.5×10^5 , the Wall Adapting Local Eddy (WALE) viscosity model (Nicoud and Ducros 1999) was adopted, and the WALE coefficient was set to be 0.5. In addition, a much finer grid system was implemented in the viscous boundary-layer region. Referring to Blocken et al. (2013), the height of the first cell from the model

surface, namely the distance from the wall normalized by the viscous length scale of the turbulent boundary layer, y^+ , was kept around 0.6 for all the cases studied. More details of the present numerical simulation method can be found in Phung (2017).

3 Results and discussion

3.1 Drag force measurements compared with the numerical results

The C_D values of the cyclist model reduced from the wind tunnel experiment for the Reynolds numbers in a range of $Re_C = 5.5 \times 10^4$ to 1.8×10^5 , together with the results of numerical simulation obtained at $Re_C = 1.1 \times 10^4$, 6.5×10^4 , and 1.5×10^5 , are presented in Fig. 4. In this figure, two sets of the C_D values obtained by the self-made balance and the commercial balance, JR3, are provided for comparison. At $Re_C = 6.5 \times 10^4$, both of the C_D values reduced from the measurements of the two balances are around 0.8, and the C_D value obtained by the numerical simulation is around 0.76. Thus, the difference is about 4.3%. However, at $Re_C = 1.5 \times 10^5$, the discrepancy between the data of the self-made balance and the JR3 balance is quite substantial, 14.9%, while the numerical result and the data obtained by JR3 are quite close. The trend that the C_D values obtained by the self-made balance appear to be higher at higher Reynolds numbers could be due to the side force generated by the cyclist model, which would introduce additional moment to the slide. However, this speculation requires further clarification. It should be mentioned that none of the C_D data in the plot have been corrected with the blockage effect of the model.

According to the data presented in Fig. 4, one can say that the C_D values are rather insensitive to the Reynolds number range studied. This observation is noted in line with the findings reported by Crouch et al. (2016b) that for the major flow structures observed in the low Reynolds number case were comparable to those at the relatively higher Reynolds numbers in the order of 10^5 . This viewpoint was also mentioned by Spohn and Gillieron (2002) with regard to a configuration of the Ahmed body that the flow structures revealed by flow visualization in a water channel at Reynolds number of 10^3 were similar to those seen at the Reynolds number of 10^6 .

The aerodynamic bluntness of the present model can be discussed with reference to the two generic models of circular cylinder and sphere. It is known from the literature that the C_D values of a smooth circular cylinder (Roshko 1993) and a smooth sphere (Schlichting 1979) for Reynolds numbers in the subcritical range of 10^4 – 10^5 are 1.2 and 0.47, respectively. Thus, the C_D values of the present model found fall between these two reference categories. Furthermore, referring to the drag coefficients of several types of the transportation vehicles (Hucho and Sovran 1993), mostly are in the range of 0.2–0.5. Apparently, the present model is bluffer than these transportation vehicles aerodynamically speaking.

3.2 Flow visualization on the model surface

Detailed features concerning the flow structures near the surface of the cyclist model can be learned from the results of flow visualization. Figure 5 presents the limiting streamline patterns revealed by the oil film method made in the wind tunnel (Fig. 5a) and the ink dots method made in the water channel (Fig. 5b),

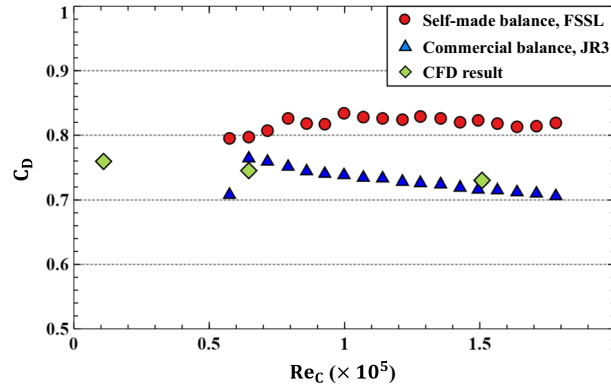


Fig. 4 Comparison of the C_D values obtained by the two balances in the wind tunnel and the numerical simulation

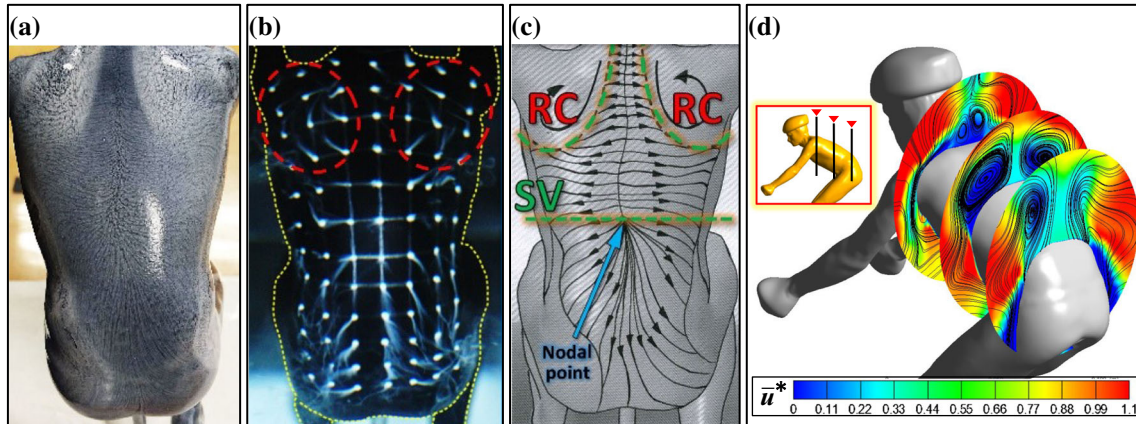


Fig. 5 Visualization at the back of the model using **a** the oil film method and **b** the ink dot method; **c** a sketch of RC and SV denoting the counter-rotating recirculation regions and a symmetric vortex pair, respectively; **d** the distributions of \bar{u}^* and the streamline patterns obtained by numerical simulation at the cross-sectional planes of $x/C = -0.14, 0.14, 0.41$

which consistently indicate that there exists a pair of counter-rotating vortices around the cyclist’s shoulder, which persist downstream over the back of the model. Based on these observations, a sketch of limiting streamlines depicting the formation of the recirculation regions, called RC, is given in Fig. 5c. The sketch further explains that the fluid in RC would be trapped and spinning in a three-dimensional manner, which would result in gathering the oil film materials on the surface. Figure 5d further provides the results of numerical simulation on the time mean flow distributions at three cross sections above the back of the cyclist model, which reveal the presence of a pair of large-scale symmetric vortices, which is indicated as SV in Fig. 5c. It is also realized that the vortex pair is developed from the junction of the cyclist neck and shoulder. Moreover, in Fig. 5c a nodal point is identified near the waist on the back, which is due to the flow reattachment on the contoured surface of the body, as induced by the vortex.

The numerical results obtained at $Re_C = 6.5 \times 10^4$ concerning the distributions of the time mean skin friction line and the pressure coefficient over the model surface are shown in Fig. 6. The pressure coefficient (C_p) is defined as $(P - P_\infty)/(0.5\rho U_\infty^2)$, where P and P_∞ denote the static pressure on the calculated point and in the incoming freestream flow, respectively. Several interesting features relevant to the flow separation phenomenon around the model are worthwhile to be mentioned below. First, a spiral focus seen at the hip of the model is coincided with a local minimum in the pressure distribution. This is physically sensible, since the flow motion near the wall is mainly governed by the pressure gradient and viscous effects. Second, a

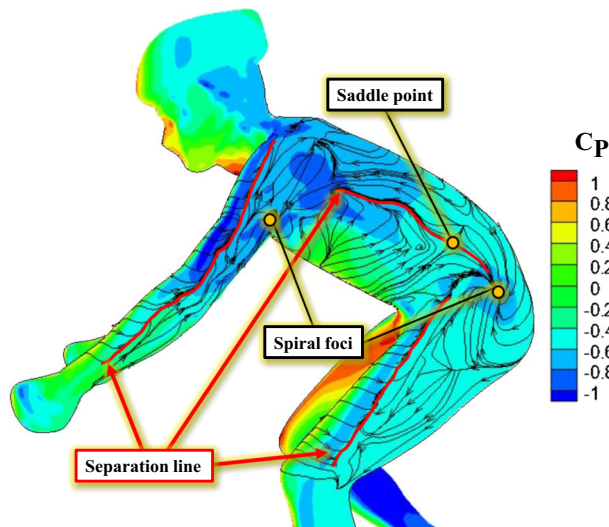


Fig. 6 Numerical results of the time-averaged distributions of skin friction line and pressure coefficient on the model surface

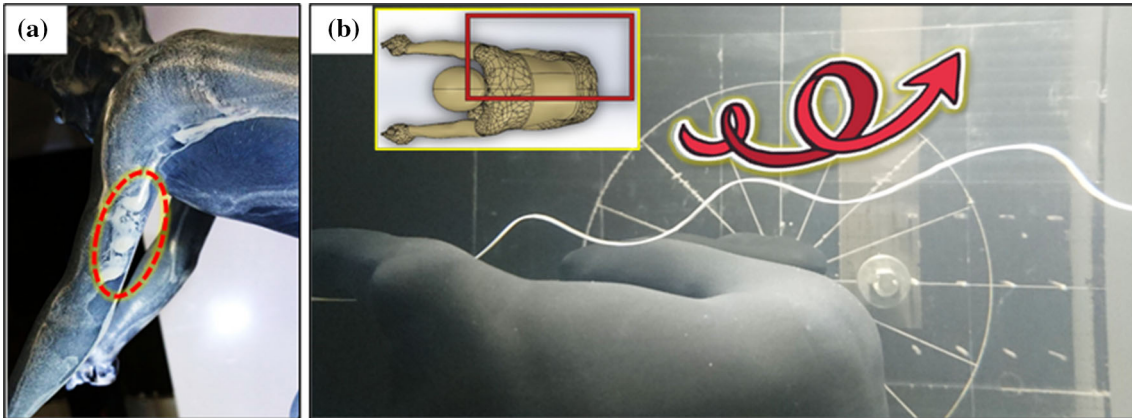


Fig. 7 **a** The oil film visualization at the left arm of the model, and **b** the dye streak released from the inside of the left arm unveiling the streamwise vortical structure around the upper body

saddle point (Lighthill 1963) marked on the left side of the upper body has an implication of flow unsteadiness, which was confirmed by flow visualization. Third, the separation lines marked on the leg, the side of the upper body and the shoulder are in fact coincided with the regions where significant adverse pressure gradients taking place on the model surface.

In Fig. 6, a spiral focus is identified at the rear of the left arm. The three-dimensional flow separation pattern can be explained due to the interference by the flow around the main body. The flow separation pattern can be further evidenced by a photograph of oil film visualization in Fig. 7a, which highlights the area on the rear side of the right arm of the cyclist. Moreover, a dye streak introduced from upstream of the arm seen in Fig. 7b provides a view of a streamwise vortex structure developed around the body, which will also be seen later in the results of the LES numerical simulation.

3.3 Wake flow development

On the PIV measurements made in the water channel with regard to the wake developed behind the cyclist model, a distribution of \bar{u}^* in the plane of $y/C = 0$ overlapped with the streamline distribution are presented in Fig. 8a for discussion. In this figure, one can identify a reversed flow region immediately below the hip; the negative \bar{u}^* values are no longer existed downstream of $x/C = 0.4$. Nevertheless, it should be pointed out that this plot does not provide much information concerning the instantaneous flow characteristics of the wake structure. Alternately, Fig. 8b presents a distribution with regard to the probability of the

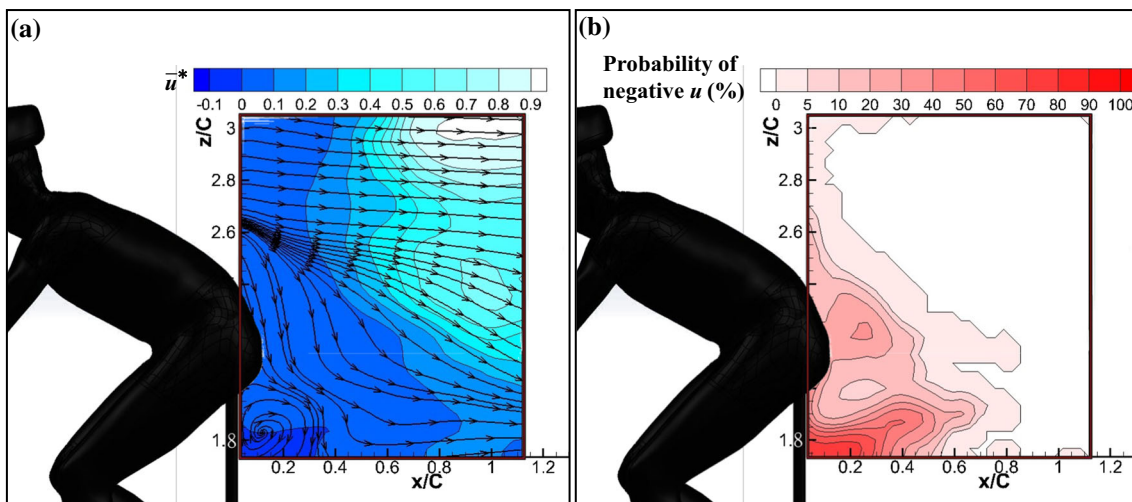


Fig. 8 The results of PIV measurements made in the water channel at $y/C = 0$. **a** The distribution of \bar{u}^* overlapped with a 2D streamline pattern, and **b** the probability distribution of the instantaneous, negative u measured

instantaneous, negative u value measured. This figure rather unveils that the probability of flow reversal does not go under 5% until $x/C = 0.8$. This finding suggested that if one would conduct the hot-wire velocity measurements in the wind tunnel, the measurements should be refrained from the region upstream of $x/C = 0.8$, since the hot-wire probe in use was unable to distinguish the forward or reversal flow.

The results of hot-wire velocity measurements made in the wind tunnel are presented in Fig. 9, in which Fig. 9a, b provides the profiles of \bar{u}^* and TI_{xyz} , respectively, along z/C at $y/C = 0$, and at the streamwise locations of $x/C=0.8, 1.2, 1.6, 2.0$ and 2.4 . As seen, the pronounced wake deficit is located around the hip region of the cyclist model. Particularly, at $x/C = 0.8$ the \bar{u}^* value around the hip region can be as low as around 0.5–0.6. Also noted in Fig. 9b, the maximum value of TI_{xyz} always takes place around the hip region for all the streamwise locations studied. Notably, at $x/C = 0.8$, the maximum TI_{xyz} value can reach about 20%. Above observations are noted in line with the findings of Crouch et al. (2014) that the momentum deficit in the region behind the hip is predominant in the wake produced by a cyclist. In addition, a significant velocity defect corresponding to the neck region is noticed in Fig. 9a, which is attributed to a junction vortex pair originated from the upper body of the model as noticed in Fig. 5.

As a counterpart of Fig. 9a, b, the distributions of \bar{u}^* and TI_{xyz} along y/C , at $z/C = 2.18$ are presented in Fig. 9c, d, respectively, for discussion. As seen, the momentum deficit on the right side ($y/C > 0$) is less severe than that on the left side, which is accompanied with lower turbulence intensity. This asymmetry is attributed to the attitude of the model featuring the asymmetric positions of the right and left legs.

Furthermore, the quantities of \bar{u}^* , TI_{xyz} , R_{xy}^* and R_{xz}^* in the y - z plane at $x/C = 1.0$ reduced from the hot-wire velocity measurements are presented in Fig. 10 for discussion. First of all, it is seen in Fig. 10a that there are two local minimum velocity regions identified in the \bar{u}^* distribution, which are associated with the streamwise coherent structures developed around the two sides of the main body like the dye streak shown in Fig. 7b. In Fig. 10b, a region of high turbulence intensity can be identified around the waist region. Basically, this plot bears the appearance similar to Fig. 10a, inferring that the turbulent fluctuations are induced by the momentum deficit in the wake.

Referring to the turbulent kinetic energy equation of motion (Tennekes and Lumley 1972), the distribution of the shearing Reynolds stress R_{xy}^* in Fig. 10c has an implication that the kinetic energy is extracted from the free stream (surrounding fluid) into the wake on both of the left and right sides of the model by

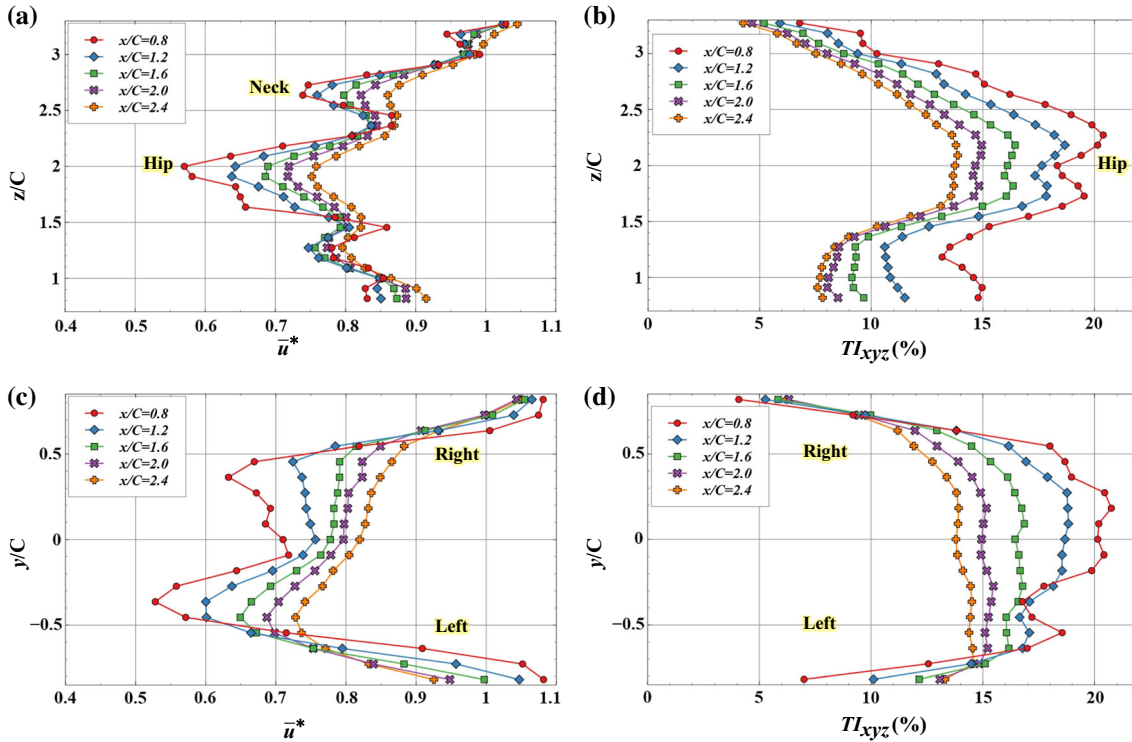


Fig. 9 The distributions of **a** \bar{u}^* and **b** TI_{xyz} with respect to z/C at $y/C = 0$, for $x/C=0.8, 1.2, 1.6, 2.0$, and 2.4 . The distributions of **c** \bar{u}^* and **d** TI_{xyz} with respect to y/C at $z/C = 2.18$, for $x/C=0.8, 1.2, 1.6, 2.0$, and 2.4

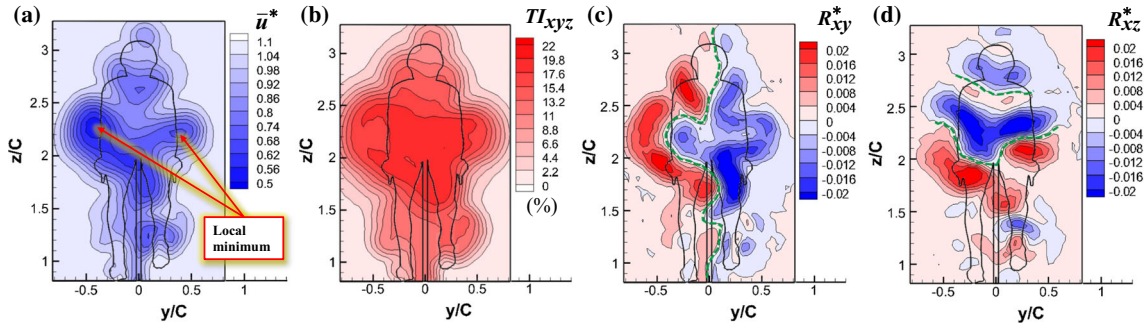


Fig. 10 The distributions of **a** \bar{u}^* , **b** TI_{xyz} , **c** R_{xy}^* , and **d** R_{xz}^* in the cross-sectional plane at $x/C = 1.0$

Table 1 The absolute values of Γ^* corresponding to the coherent vortices marked in Fig. 11

Label	$ \Gamma^* , (\times 10^{-2})$	Label	$ \Gamma^* , (\times 10^{-2})$
①	0.9993	⑧	2.8816
②	0.3077	⑨	0.8935
③	9.7730	⑩	3.6945
④	5.8479	⑪	2.3093
⑤	2.3438	⑫	4.9848
⑥	3.7465	⑬	2.6800
⑦	1.6206	⑭	1.5742

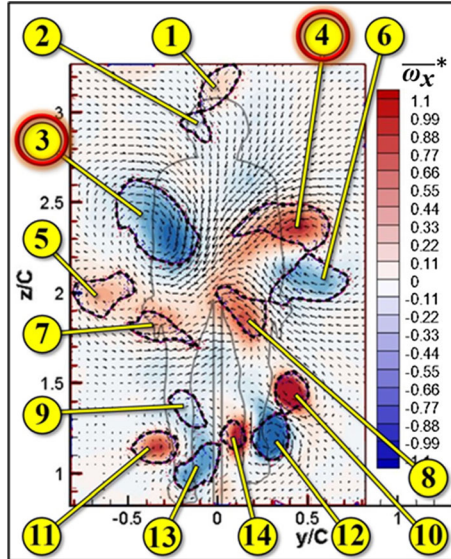


Fig. 11 The 2D velocity vector plot in the cross-sectional plane of $x/C = 1.0$, together with the corresponding $\overline{\omega}_x^*$ distribution. The coherent vortices identified are marked with the numbers

means of turbulent fluctuations. A dashed line indicated in Fig. 10c marks the division between the regions corresponding to the positive and negative values of R_{xy}^* measured. As a counterpart of Fig. 10c, d presents the distribution of R_{xz}^* that the positive R_{xz}^* values are seen in the region above the hip, whereas the negative R_{xz}^* values are seen in the region below. Again, this appearance infers that the kinetic energy is extracted from the free stream due to this shearing action into the wake region. Accordingly, the pronounced turbulent fluctuations seen in the region behind the hip (Fig. 10b) is involved with the transportation of the kinetic energy due to the shearing Reynolds stresses of R_{xy}^* and R_{xz}^* .

To further examine the characteristics of large-scale flow structures in the wake, a 2D velocity vector plot in the cross-sectional plane of $x/C = 1.0$, together with the corresponding $\overline{\omega}_x^*$ distribution are

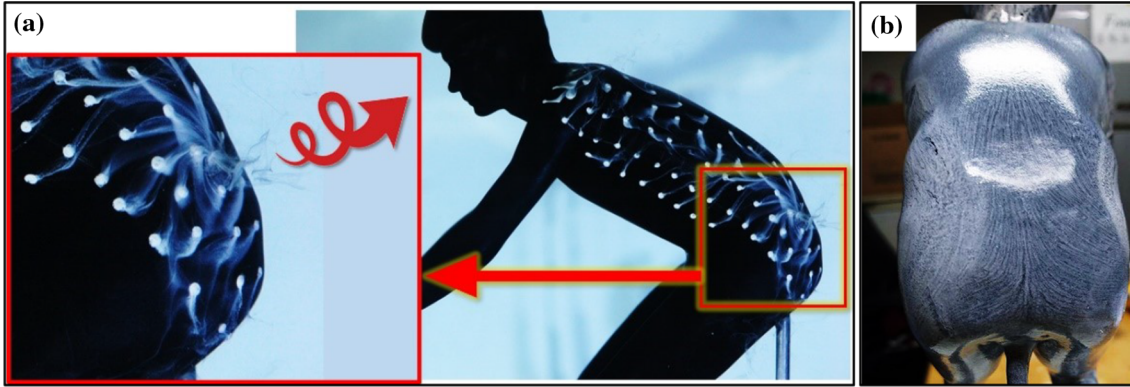


Fig. 12 The coherent vortices near the hip revealed by **a** the ink dots method, and **b** the oil film pattern about the hip region

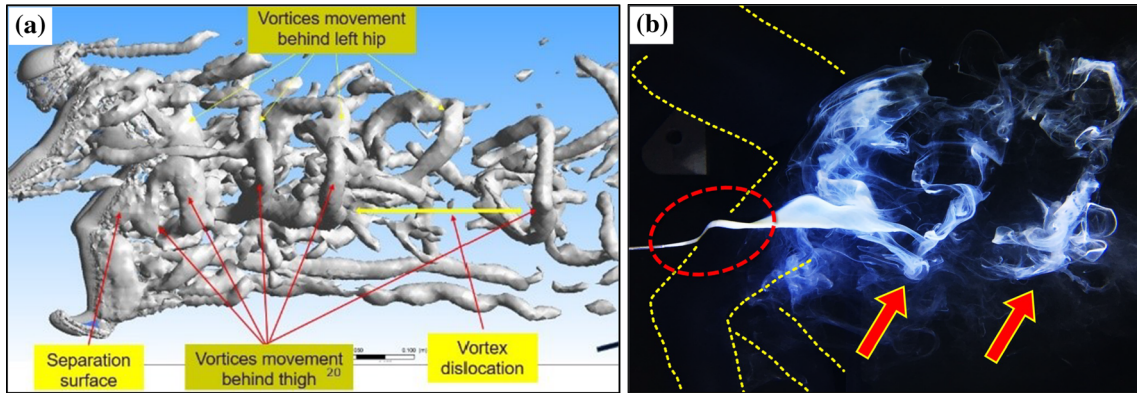


Fig. 13 **a** A snapshot view of large-scale eddies in the near-wake region at $Re_C = 6.5 \times 10^4$ obtained by the LES numerical simulation, and **b** the dye streak visualization obtained in the water channel unveiling the shedding flow structures originated from the hip and upper leg regions

presented in Fig. 11. In the figure, $\overline{\omega}_x^*$ is indicated by red and blue colors with respect to the positive and negative values. Moreover, the regions of significant $\overline{\omega}_x^*$ identified by the λ_2 -criterion are marked, which are called the streamwise coherent vortices herein. The absolute values of I^* corresponding to the coherent vortices identified by numbers are listed in Table 1 for reference. It is noteworthy that the predominant ones are seen around the upper body, although the vortices behind the legs are also noticeable.

The coherent vortices marked as nos. 3 and 4 are the most prominent ones, which appear as a large-scale vortex pair similar to the trailing vortex pair behind the automobile or Ahmed body (Hucho and Sovran 1993). As noticed, this vortex pair is involved with the spiral flow separations developed on the hip surface, which can be seen from the ink dots visualization in Fig. 12a as well as the numerical result in Fig. 6 shown previously. Globally speaking, the attached flow along the center of the back of the model realized from Fig. 5 as well as the flow visualization photograph in Fig. 12b induces a downwash motion. Consequently, the large-scale counter-rotating streamwise vortices are developed around the main body.

The wake development behind the cyclist model can be further explained with Fig. 13. Figure 13a provides a snapshot view of the LES numerical results depicting the development of the large-scale vortical structures in the near-wake region. Two interesting features are worth mentioning below. First, the large-scale eddies initiated from the model surface are intimately linked with the flow separations from the model surface. Notably, the separated flow seen from the left arm interact with the vortices around the left side of the upper body, that is the large-scale streamwise vortical flow unveiled by the numerical results of the time mean flow distribution in Fig. 5d. In Fig. 13a, the vortices shed from the head and the upper left leg are also identifiable. Second, slightly downstream of the model, the large-scale eddies evolve into loop structures with various orientations. For comparison, Fig. 13b presents a photograph of dye visualization unveiling the shedding flow structures from the upper left leg, which was obtained in the water channel experiment. While such loop structures are commonly seen in the wake behind a three-dimensional bluff body, such as flow

over a circular disk (Miao et al. 1997) or a sphere (Taneda 1978), the present ones in Fig. 13a appear to be much more complex. This is due to that multiple streamwise coherent vortices were originated from different parts of the contoured body.

4 Conclusions

In this study, we assume that the flow characteristics around the cyclist model be insensitive to the Reynolds numbers over the range obtained in the water channel and wind tunnel experiments, particularly the large-scale flow structures revealed by flow visualization in these two facilities. The results obtained indicate that the numerical approach can complement the experimental method satisfactorily in obtaining the drag coefficient as well as gaining the insightful information of the aerodynamic flow around the cyclist body. Specifically, the drag coefficients obtained by experiment and numerical simulation are in good agreement. The variations in drag coefficients for Reynolds numbers of 10^4 – 10^5 are rather insignificant, inferring that the aerodynamic flow characteristics remains insensitive to the Reynolds numbers in this range.

A major finding is that in the near-wake region, the flow consists of multiple streamwise coherent vortices, which are interacting strongly and induce highly turbulent mixing of momentum. The most significant vortex pair found is around the upper body, whose scale is comparable to the waist of the body. The development of this vortex pair is associated with the downwash flow along the back of the cyclist body, whereas the separated flows are seen at the sides of the upper body, the hip surface and the rear sides of both arms. Furthermore, the region behind the hip region is found with the pronounced deficit in momentum. As noted, the momentum deficit in the wake region induces turbulent mixing strongly, which promotes the shearing Reynolds stresses to entrain the freestream fluid into the wake region.

In addition to the significant amount of drag resulted in the wake behind the hip, the drag due to the arms, legs and neck is noticeable. This can be realized from Fig. 11, in which the coherent structures identified as nos. 7–14 are associated with the legs of the cyclist, the ones of nos. 5 and 6 are associated with the arms, and those of nos. 1 and 2 are associated with neck and head. In comparison with the findings of Defraeye et al. (2011) with regard to the drag components corresponding the 19 segments of a cyclist model at the upright, dropped and time trial positions, the findings of the significant contributions due to the head, arms and legs in the two studies are in good agreement. However, the contribution due to the pronounced momentum deficit behind the hip, which is noted in the present study, was not particularly mentioned in Defraeye et al. (2011). The difference is attributed to the configurations of the two cyclist models and their riding postures. In fact, this difference enlightens a fundamental issue in cycling aerodynamics that the contoured shape and posture of a cyclist are deemed the utmost importance as far as the reduction of drag is concerned.

Acknowledgements The authors are grateful to GIANT Bicycle Inc., Taiwan, for providing the cyclist model data. In addition, the first author (JJM) would like to acknowledge the funding support of Ministry of Science and Technology under the project MoST 107-2627-H-006-003—during the preparation of this manuscript.

Open Access This article is distributed under the terms of the Creative Commons Attribution 4.0 International License (<http://creativecommons.org/licenses/by/4.0/>), which permits unrestricted use, distribution, and reproduction in any medium, provided you give appropriate credit to the original author(s) and the source, provide a link to the Creative Commons license, and indicate if changes were made.

References

- Bandet JS, Perisol AG (1991) Random data analysis and measurement procedures, 2nd edn. Wiley, New York
- Blocken B, Defraeye T, Koninckx E, Carmeliet J, Hespel P (2013) CFD simulations of the aerodynamic drag of two drafting cyclists. *Comput Fluids* 71:435–445
- Blocken B, van Druenen T, Toparlar Y, Andrienne T (2018) Aerodynamic analysis of different cyclist hill descent positions. *J Wind Eng Ind Aerodyn* 181:27–45
- Chen Q, Zhong Q, Qi M, Wang X (2015) Comparison of vortex identification criteria for planar velocity fields in wall turbulence. *Phys Fluids* 27(8):085101
- Chowdhury H, Alam F (2014) An experimental investigation on the aerodynamic drag coefficient and surface roughness properties of sport textiles. *J Text Inst* 105(4):414–422
- Crouch TN, Burton D, Brown NAT, Thompson MC, Sheridan J (2014) Flow topology in the wake of a cyclist and its effect on aerodynamic drag. *J Fluid Mech* 748:5–35

- Crouch TN, Burton D, Thompson MC, Brown NAT, Sheridan J (2016a) Dynamic leg-motion and its effect on the aerodynamic performance of cyclists. *J Fluids Struct* 65:121–137
- Crouch TN, Burton D, Venning JA, Thompson MC, Brown NAT, Sheridan J (2016b) A comparison of the wake structures of scale and full-scale pedaling cycling models. *Procedia Eng* 147:13–19
- Debraux P, Grappe F, Manolova AV, Bertucci W (2011) Aerodynamic drag in cycling: methods of assessment. *Sports Biomech* 10:197–218
- Defraeye T, Blocken B, Koninckx E, Hespel P, Carmeliet J (2010a) Aerodynamic study of different cyclist positions: CFD analysis and full-scale wind tunnel tests. *J Biomech* 43:1262–1268
- Defraeye T, Blocken B, Koninckx E, Hespel P, Carmeliet J (2010b) Computational fluid dynamics analysis of cyclist aerodynamics: performance of different turbulence-modelling and boundary-layer modelling approaches. *J Biomech* 43:2281–2287
- Defraeye T, Blocken B, Koninckx E, Hespel P, Carmeliet J (2011) Computational fluid dynamics analysis of drag and convective heat transfer of individual body segments for different cyclist positions. *J Biomech* 44:1695–1701
- Defraeye T, Blocken B, Koninckx E, Hespel P, Verboven P, Nicolai B, Carmeliet J (2014) Cyclist drag in team pursuit: influence of cyclist sequence, stature, and arm spacing. *J Biomech Eng Trans ASME* 136:011005-1
- Griffith MD, Crouch TN, Thompson MC, Burton D, Sheridan J, Brown NA (2014) Computational fluid dynamics study of the effect of leg position on cyclist aerodynamic drag. *J Fluids Eng* 136(10):101–105
- Hsu XY, Miao JJ, Tsai JH, Tsai ZX, Lai YH, Ciou YS, Shen PT, Chuang PC, Wu CM (2019) The aerodynamic roughness of textile materials. *J Text Inst* 110(5):771–779
- Hucho WH, Sovran G (1993) Aerodynamics of road vehicles. *Annu Rev Fluid Mech* 25:485–537
- Jeong J, Hussain F (1995) On the identification of a vortex. *J Fluid Mech* 285:69–94
- Kyle CR, Burke E (1984) Improving the racing bicycle. *Mech Eng* 106:34–45
- Li SR (2017) Investigation on wake structure of a cyclist model at the hoods position. Master Thesis, National Cheng Kung University, Tainan, Taiwan
- Li SR, Miao JJ, Phung MV, Tsai ZX, Lin SY (2017) Investigation on wake structure of a cyclist model at the hoods position. In: *The 14th Asian symposium on visualization*, Beijing, 22–26 May 2017
- Lighthill ML (1963) Introduction, boundary layer theory. In: Rosenhead L (ed) *Laminar boundary layers*, Chapter II. Oxford University Press, Oxford
- Lukes RA, Chin SB, Haake SJ (2005) The understanding and development of cycling aerodynamics. *Sports Eng* 8(2):59–74
- McMillan OJ, Ferziger JH (1979) Direct testing of subgrid-scale models. *AIAA J* 17:1340–1346
- Miao JJ, Leu TS, Lin TW, Chou JH (1997) On vortex shedding behind a circular disk. *Exp Fluids* 23:225–233
- Nicoud F, Ducros F (1999) Subgrid-scale stress modelling based on the square of the velocity gradient tensor. *Flow Turbul Combust* 62:183–200
- Oggiano L, Sætran L, Løsetp S, Winther R (2007) Reducing the athlete's aerodynamic resistance. *J Comput Appl Mech* 8(2):163–173
- Oggiano L, Troynikov O, Konopov I, Subic A, Alam F (2009) Aerodynamic behavior of single sport jersey fabrics with different roughness and cover factors. *Sports Eng* 12(1):1–16
- Parker PA, Morton M, Draper N, Line W (2001) A single vector force calibration method featuring the modern design of experiments. In: *Proceedings of the 39th AIAA aerospace sciences meeting and exhibition*, AIAA-2001-0170, Reno, NV
- Phung MV (2017) Aerodynamic study of cycling hood position by using large eddy simulation methods. Master Thesis, National Cheng Kung University, Tainan, Taiwan
- Roshko A (1993) Perspectives on bluff body aerodynamics. *J Wind Eng Ind Aerodyn* 49:70–100
- Schlichting H (1979) *Boundary-layer theory*, 7th edn. McGraw-Hill, New York
- Smagorinsky J (1963) General circulation experiments with primitive equations. *Mon Weather Rev* 91(3):99–164
- Spohn A, Gillieron P (2002) Flow separations generated by a simplified geometry of an automotive vehicle. In: *IUTAM symposium on unsteady separated flows*, Toulouse, 8–12 April 2002
- Taneda S (1978) Visual observations of the flow past a sphere at Reynolds numbers between 10^4 and 10^6 . *J Fluid Mech* 85(1):187–192
- Tennekes H, Lumley JL (1972) *A first course in turbulence*. MIT Press, Cambridge
- Tsai ZX, Miao JJ, Chen TL, Lai YH, Wong H (2016) Balance design for drag measurement. In: *The 11th international symposium on advanced science and technology in experimental mechanics*, Ho Chi Minh, 1–4 Nov 2016